Temperature profiles of young disk-like structures The case of IRAS 16293A star

van't Hoff, Merel L. R.; van Dishoeck, Ewine F.; Jorgensen, Jes K.; Calcutt, Hannah

Published in:
Astronomy & Astrophysics

DOI:
10.1051/0004-6361/201936839

Publication date:
2019

Document version
Publisher's PDF, also known as Version of record

A&A 633, A7 (2020)
https://doi.org/10.1051/0004-6361/201936839

Astronomy & Astrophysics

Temperature profiles of young disk-like structures

The case of IRAS 16293A*

Merel L. R. van 't Hoff[1], Ewine F. van Dishoeck[1,2], Jes K. Jørgensen[3], and Hannah Calcutt[4]

[1] Leiden Observatory, Leiden University, PO Box 9513, 2300 RA Leiden, The Netherlands
e-mail: vthoff@strw.leidenuniv.nl
[2] Max-Planck-Institut für Extraterrestrische Physik, Giessenbachstrasse 1, 85748 Garching, Germany
[3] Niels Bohr Institute, University of Copenhagen, Øster Voldgade 5–7, 1350 Copenhagen K., Denmark
[4] Department of Space, Earth and Environment, Chalmers University of Technology, 41296 Gothenburg, Sweden

Received 3 October 2019 / Accepted 1 November 2019

ABSTRACT

Context. Temperature is a crucial parameter in circumstellar disk evolution and planet formation because it governs the resistance of the gas to gravitational instability and sets the chemical composition of the planet-forming material.
Aims. We set out to determine the gas temperature of the young disk-like structure around the Class 0 protostar IRAS 16293–2422A.
Methods. We used Atacama Large Millimeter/submillimeter Array (ALMA) observations of multiple H_2CS $J = 7 - 6$ and $J = 10 - 9$ lines from the Protostellar Interferometric Line Survey (PILS) to create a temperature map for the inner ∼200 AU of the disk-like structure. This molecule is a particularly useful temperature probe because transitions between energy levels with different K_a quantum numbers operate only through collisions.
Results. Based on the H_2CS line ratios, the temperature is between ∼100–175 K in the inner ∼150 AU, and drops to ∼75 K at ∼200 AU. At the current resolution (0.5″ ∼70 AU), no jump is seen in the temperature at the disk–envelope interface.
Conclusions. The temperature structure derived from H_2CS is consistent with envelope temperature profiles that constrain the temperature from 1000 AU scales down to ∼100 AU, but does not follow the temperature rise seen in these profiles at smaller radii. Higher angular resolution observations of optically thin temperature tracers are needed to establish whether cooling by gas-phase water, the presence of a putative disk, or the dust optical depth influences the gas temperature at $\lesssim$100 AU scales. The temperature at 100 AU is higher in IRAS 16293A than in the embedded Class 0/I disk L1527, consistent with the higher luminosity of the former.

Key words. stars: formation – stars: protostars – ISM: molecules – ISM: individual objects: IRAS 16293–2422

1. Introduction

Disks form around young stars due to conservation of angular momentum during the gravitational collapse of a dense core (Cassen & Moosman 1981) and many disks have been reported around T Tauri and Herbig stars (Class II objects, e.g., Andrews & Williams 2005; Ansdell et al. 2016). Disk-like structures are also observed in continuum emission toward embedded protostars (Class 0 and I; e.g., Jørgensen et al. 2009; Tobin et al. 2016), but Keplerian rotation has been established for only a handful of the youngest Class 0 sources (Tobin et al. 2012; Murillo et al. 2013; Lindberg et al. 2014; Codella et al. 2014; Yen et al. 2017). The formation of rotationally supported disks thus remains poorly constrained (see, e.g., Li et al. 2014, for a review), as well as their physical and chemical structure. However, it is now becoming clear that planet formation already starts in these young disks. The mass of mature protoplanetary disks seems too low to form the planetary systems that we observe (e.g., Ansdell et al. 2016; Manara et al. 2018), while younger disks are more massive (Tychoniec et al. 2018; Williams et al. 2019). This suggests that by the Class II stage, material has grown to larger bodies that cannot be observed at (sub-)millimeter wavelengths. The first steps of grain growth have indeed been observed in disks that have not yet fully emerged from their envelope (Kwon et al. 2009; Jørgensen et al. 2009; Pagani et al. 2010; Foster et al. 2013; Miotello et al. 2014; Harsono et al. 2018). Young embedded disks thus provide the initial conditions for planet formation.

An important unknown for young disks is the temperature structure because this governs whether they are gravitationally unstable, and thus capable of forming planets through gravitational instabilities (e.g., Boss 1997; Boley 2009), or prone to luminosity outbursts (Vorobyov 2009). In addition, knowledge of temperature is required to derive disk masses, and thus the amount of material available for planet formation, from continuum observations. Finally, the temperature sets the chemical composition of the planet-forming material, for example, through the sequential freeze-out of volatiles as the temperature decreases at larger distances from the central star (e.g., Öberg et al. 2011).

The radial onset of CO freeze-out, the CO snowline, has been located in several protoplanetary disks, revealing that these disks have a large reservoir of cold ($\lesssim$25 K) gas with CO freeze-out starting at a few tens to ∼100 AU from the star (Qi et al. 2013, 2015, 2019; Öberg et al. 2015; Dutrey et al. 2017). In contrast to these mature disks, the young embedded disk in L1527 shows no signs of CO freeze-out (van 't Hoff et al. 2018) in agreement with model predictions (Harsono et al. 2015). But whether all

* Reduced datacubes and images are only available at the CDS via anonymous ftp to cdsarc.u-strasbg.fr (130.79.128.5) or via http://cdsarc.u-strasbg.fr/viz-bin/cat/J/A+A/633/A7

young disks are warm and when they start to cool remain open questions. Moreover, while mature disks can be described with a power law midplane temperature profile, this is not necessarily the case for embedded disks as material may be heated in shocks at the disk–envelope interface (centrifugal barrier; e.g., Sakai et al. 2014). Here, we study the gas temperature of the young disk-like structure around one component of the Class 0 protostellar system IRAS 16293–2422.

IRAS 16293–2422 (hereafter IRAS 16293) is a well-studied deeply embedded protostellar binary in the L1689 region in ρ Ophiuchus (d ~140 pc; Dzib et al. 2018). The separation between the two components, often referred to as IRAS 16293A and IRAS 16293B is ~5.1″ (~715 AU; Wootten 1989; Mundy et al. 1992; Looney et al. 2000; Chandler et al. 2005; Pech et al. 2010), and both protostars show compact millimeter continuum emission on 100 AU scales (Looney et al. 2000; Schöier et al. 2004). IRAS 16293A has a velocity gradient in the NE-SW direction that could be attributed to a rotating disk viewed edge-on, while rotating motion is hardly detected toward source B, suggesting a near face-on orientation (Pineda et al. 2012; Favre et al. 2014; Oya et al. 2016). The protostellar masses are estimated to be $M_A \sim 1 M_\odot$ and $M_B \sim 0.1 M_\odot$ (Bottinelli et al. 2004; Caux et al. 2011), but two continuum sources (~0.38″ or ~50 AU separation) have been detected toward IRAS 16293A at centimeter and millimeter wavelengths, suggesting that IRAS 16293A itself may be a binary as well (Wootten 1989; Chandler et al. 2005; Pech et al. 2010), or even a triple system if A1 is in fact a very tight binary (Hernández-Gómez et al. 2019).

Existing temperature structures for IRAS 16293 are based on modeling of continuum emission (e.g., Schöier et al. 2002) and spatially unresolved observations of water and oxygen lines with the Infrared Space Observatory (ISO), assuming an infalling envelope around a single protostar (e.g., Ceccarelli et al. 2000; Crimier et al. 2010). The first detailed 3D modeling of the continuum, ^{13}CO and C^{18}O emission, including two radiation sources (~18 $L_\odot$ for source A and ~3 $L_\odot$ for source B), was presented by Jacobsen et al. (2018). All these temperature profiles are consistent with water ice desorption (~100 K) at ~100–150 AU.

IRAS 16293 was the first low-mass protostellar envelope in which complex organics were detected (van Dishoeck et al. 1995; Cazaux et al. 2003). The ALMA Protostellar Interferometric Line Survey (PILS; an unbiased spectral survey between 329 and 363 GHz at 0.5″ resolution presented by Jørgensen et al. 2016) fully revealed the chemical richness of this source with approximately one line detected per 3 km s^{-1}. The large frequency range covered also makes the PILS data very well-suited to study the temperature structure through ratios of line emission from different transitions within one molecule. Particularly good tracers of temperature are H_2CO and H_2CS (e.g., Mangum & Wootten 1993; van Dishoeck et al. 1993, 1995) for which multiple lines are covered by the PILS survey (Persson et al. 2018).

The molecules H_2CO and H_2CS are slightly asymmetric rotors and have their energy levels designated by the quantum numbers J, K_a, and K_c. Since transitions between energy levels with different K_a values operate only through collisional excitation, line ratios involving different K_a ladders are good tracers of the kinetic temperature (e.g., Mangum & Wootten 1993; van Dishoeck et al. 1993, 1995). Moreover, transitions from different K_a levels connecting the same J levels are closely spaced in frequency such that they can be observed simultaneously. Therefore, line ratios from K_a transitions within the same ΔJ transition can provide a measure of the kinetic temperature unaffected by relative pointing uncertainties, beam-size differences, and absolute calibration uncertainties.

In this paper we focus on H_2CS to derive a temperature profile for the disk-like structure around IRAS 16293A because too few unblended lines were available for H_2CO and $H_2^{13}CO$, and the H_2CO and D_2CO lines are optically thick. The observations are briefly described in Sect. 2. In Sect. 3 we present temperature maps based on H_2CS line ratios and rotation diagrams, showing that the temperature remains between ~100 and ~175 K out to ~150 AU, consistent with envelope temperature profiles, but flattens in the inner ~100 AU. At the current spatial resolution of the data, no jump in temperature is seen at the disk–envelope interface. This temperature profile is further discussed in Sect. 4 and the conclusions are summarized in Sect. 5.

2. Observations

The Protostellar Interferometric Line Survey (PILS) is an unbiased spectral survey of the low-mass protobinary IRAS 16293 with the Atacama Large Millimeter/submillimeter Array (ALMA) covering frequencies between 329.147 and 362.896 GHz in Band 7 (project ID: 2013.1.00278.S). Multiple lines from H_2CO, H_2CO isotopologues and H_2CS fall within this spectral range. The ΔJ transitions with multiple K_a transitions available are listed in Table A.1. The transition frequencies and other line data were taken from the CDMS database (Müller et al. 2001, 2005). The H_2CO entries are based on Bocquet et al. (1996), Cornet & Winnewisser (1980), Brünken et al. (2003), and Müller & Lewen (2017), and the $H_2^{13}CO$ entries are taken from Müller et al. (2000). Entries of the deuterated isotopologues are based on Dangoisse et al. (1978), Bocquet et al. (1999), and Zakharenko et al. (2015). H_2CS data are provided by Fabricant et al. (1977), Maeda et al. (2008), and Müller et al. (2019).

The data have a spectral resolution of 0.2 km s^{-1} (244 kHz), a restoring beam of 0.5″ (~70 AU), and a sensitivity of 7–10 mJy beam^{-1} channel^{-1}, or ~5 mJy beam^{-1} km s^{-1}, across the entire frequency range. The phase center is located between the two continuum sources at α(J2000) = 16^{h}32^{m}22^s.72; δ(J2000) = −24°28′34.″3. In this work we focus on the A source (α(J2000) = 16^{h}32^{m}22^s.873; δ(J2000) = −24°28′36.″54). A detailed description of the data reduction and continuum subtraction can be found in Jørgensen et al. (2016).

The PILS program also contains eight selected windows in Band 6 (~230 GHz) at the same angular resolution as the Band 7 data (0.5″; project ID: 2012.1.00712.S). These data have a spectral resolution of 0.15 km s^{-1} (122 kHz) and a sensitivity of ~4 mJy beam^{-1} channel^{-1}, or ~1.5 mJy beam^{-1} km s^{-1}. The data reduction proceeded in the same manner as the Band 7 data (Jørgensen et al. 2016). Several H_2CS $J_{K_aK_c} = 7_{xx} - 6_{xx}$ transitions are covered by this spectral setup (see Table A.1).

IRAS 16293 was also observed at 0.5″ resolution by program 2016.1.01150.S (PI: Taquet). This dataset has a spectral resolution of 0.15 km s^{-1} (122 kHz) and a sensitivity of ~1.3 mJy beam^{-1} channel^{-1}, or ~0.5 mJy beam^{-1} km s^{-1}, and covers the H_2CS $7_{1,7} - 6_{1,6}$ transition (Table A.1). The data reduction is described in Taquet et al. (2018).

3. Results

3.1. Kinematics

The incredible line-richness of IRAS 16293 (on average one line per 3.4 MHz) means that many lines are blended (e.g., Jørgensen et al. 2016). In addition, the large velocity gradient due to the near edge-on rotating structure around the A source (~6 km s^{-1}; Pineda et al. 2012; Favre et al. 2014) results in varying line widths

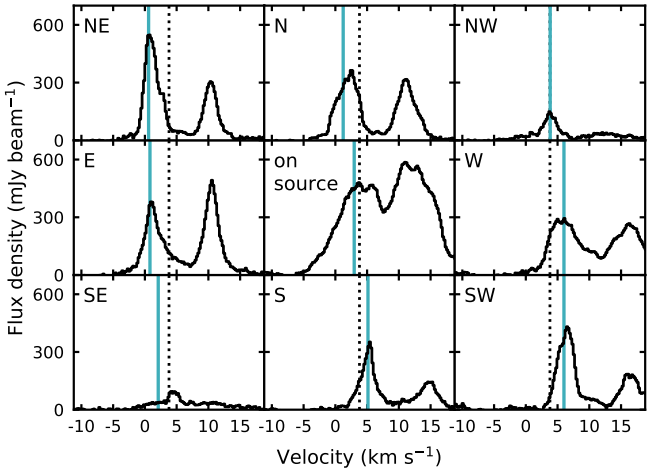

Fig. 1. Spectra of the H_2CS $10_{0,10}$–$9_{0,9}$ line at nine positions toward IRAS 16293A illustrating the variation in line blending across the source. *Central panel*: spectrum in the central pixel (continuum peak); the other spectra are taken at a beam offset (0.5″) in the different directions denoted in the top left corner of each panel. The vertical dotted line marks the system velocity of 3.8 km s^{-1}, and the vertical blue solid line indicates the peak velocity from the CH_3OH line used to isolate the target lines (in this case H_2CS $10_{0,10}$–$9_{0,9}$).

and hence varying degrees of blending at different positions (see Fig. 1). Therefore, we make use of the method outlined in Calcutt et al. (2018) to isolate the formaldehyde and thioformaldehyde lines: the peak velocity in each pixel is determined using a bright methanol transition ($7_{3,5}$–$6_{4,4}$ at 337.519 GHz) and this velocity map is then used to identify the target lines listed in Appendix A.

Of the 18 formaldehyde and 15 thioformaldehyde lines, only the H_2CO $5_{1,5}$–$4_{1,4}$, $H_2^{13}CO$ $5_{2,4}$–$4_{2,3}$, $H_2^{13}CO$ $5_{4,1}$–$4_{4,0}$, D_2CO $6_{3,4}$–$5_{3,3}$, and H_2CS $7_{2,5}$–$6_{2,4}$ lines can be fully isolated. Figure 2 shows the Velocity-corrected INtegrated Emission (VINE) map for H_2CS $7_{2,5}$–$6_{2,4}$, that is, the moment zero map but integrated over different velocities in each pixel (Calcutt et al. 2018), as well as a map of the corresponding peak velocities. The emission shows an elongated structure in the northeast–southwest direction along the velocity gradient. The $H_2^{13}CO$ $5_{1,5}$–$4_{1,4}$, $H_2^{13}CO$ $5_{2,3}$–$4_{2,2}$, D_2CO $6_{2,5}$–$5_{2,4}$, and H_2CS $10_{2,9}$–$_{2,8}$ lines are severely blended (<4 MHz to another line) and were excluded from the analysis (see Table A.1 for details). All other lines are blended to some degree. In most cases this means that one or both of the line wings in the central pixels (∼0.5″ radius) overlap with the wing of another line.

An overview of the 14 H_2CS lines is shown in Fig. 3 in the form of position–velocity (pv) diagrams along the major axis of the disk-like structure (PA = 65°; Oya et al. 2016) and spectra extracted ∼0.5″ to the northeast of the source center (see Fig. 2). Similar pv diagrams for H_2CO, $H_2^{13}CO$, and D_2CO are presented in Appendix B. All lines show signs of rotation, that is, low velocities at large angular offsets and high velocities closer to the source center. H_2CO and H_2CS emission extends out to ≳2″, while emission from the less abundant isotopologues $H_2^{13}CO$ and D_2CO is more compact (≲1″), probably due to sensitivity. The emission also becomes more compact for transitions with higher upper level energies, which are expected to trace the warmest inner region. The H_2CO lines show redshifted absorption for velocities slightly above the systemic velocity of 3.8 km s^{-1}.

Based on large shifts in velocity from the systemic velocity (up to 14 km s^{-1}) for the H_2CS $7_{0,7}$–$6_{0,6}$ line, Oya et al. (2016) suggested that a Keplerian disk may be present inside the

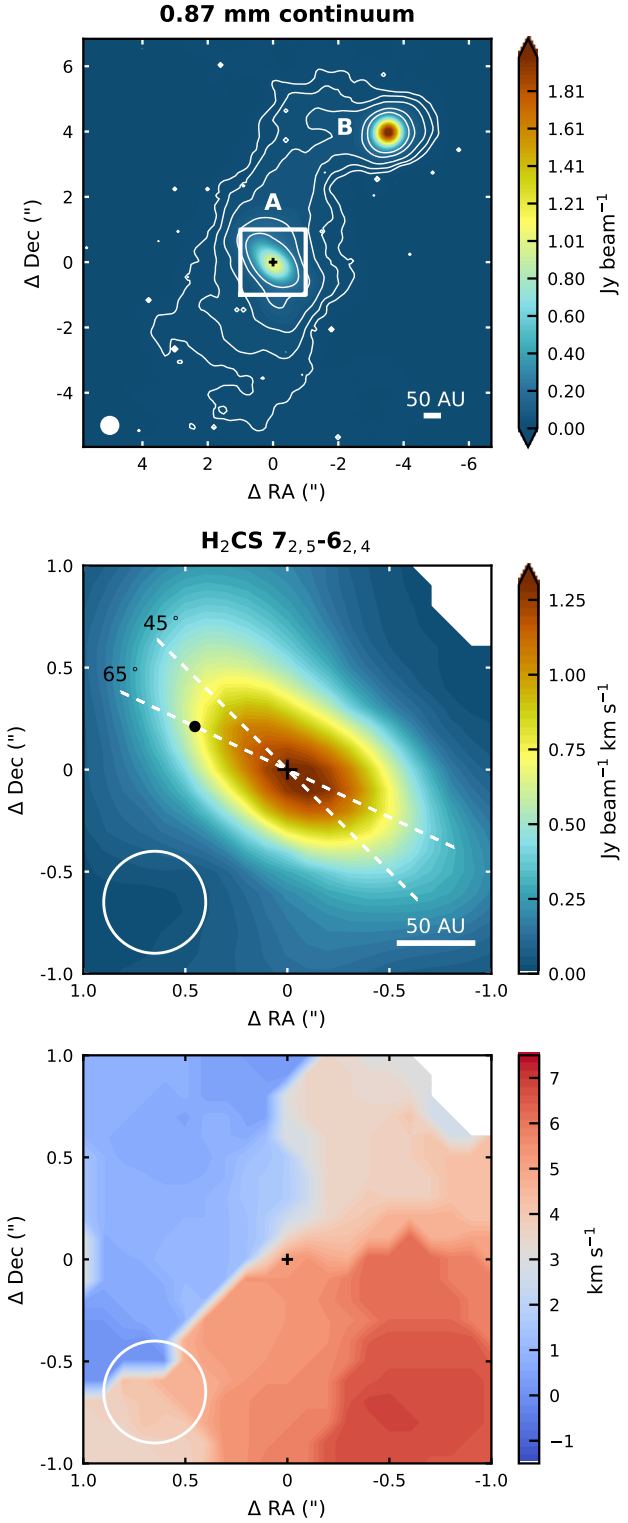

Fig. 2. Continuum image of IRAS 16293 at 0.87 mm (*top panel*) with contour levels at 0.5, 1, 2, 5, and 10% of the peak flux. The white box indicates the region around the A source for which the velocity-corrected integrated emission (VINE) map of the H_2CS $7_{2,5}$–$6_{2,4}$ line at 240.549 GHz (E_u = 99 K) is shown in the *middle panel*, and the peak velocity at each position in the *bottom panel*. The continuum peak position of IRAS 16293A is marked with a cross in all panels and the beam is depicted in the lower left corners. The white lines in the *middle panel* indicate the position angle of the major axis of the disk-like structure found by Oya et al. (2016) (65°) and our by-eye best matching position angle of 45°. The black circle gives the position where the spectra in Fig. 3 are extracted.

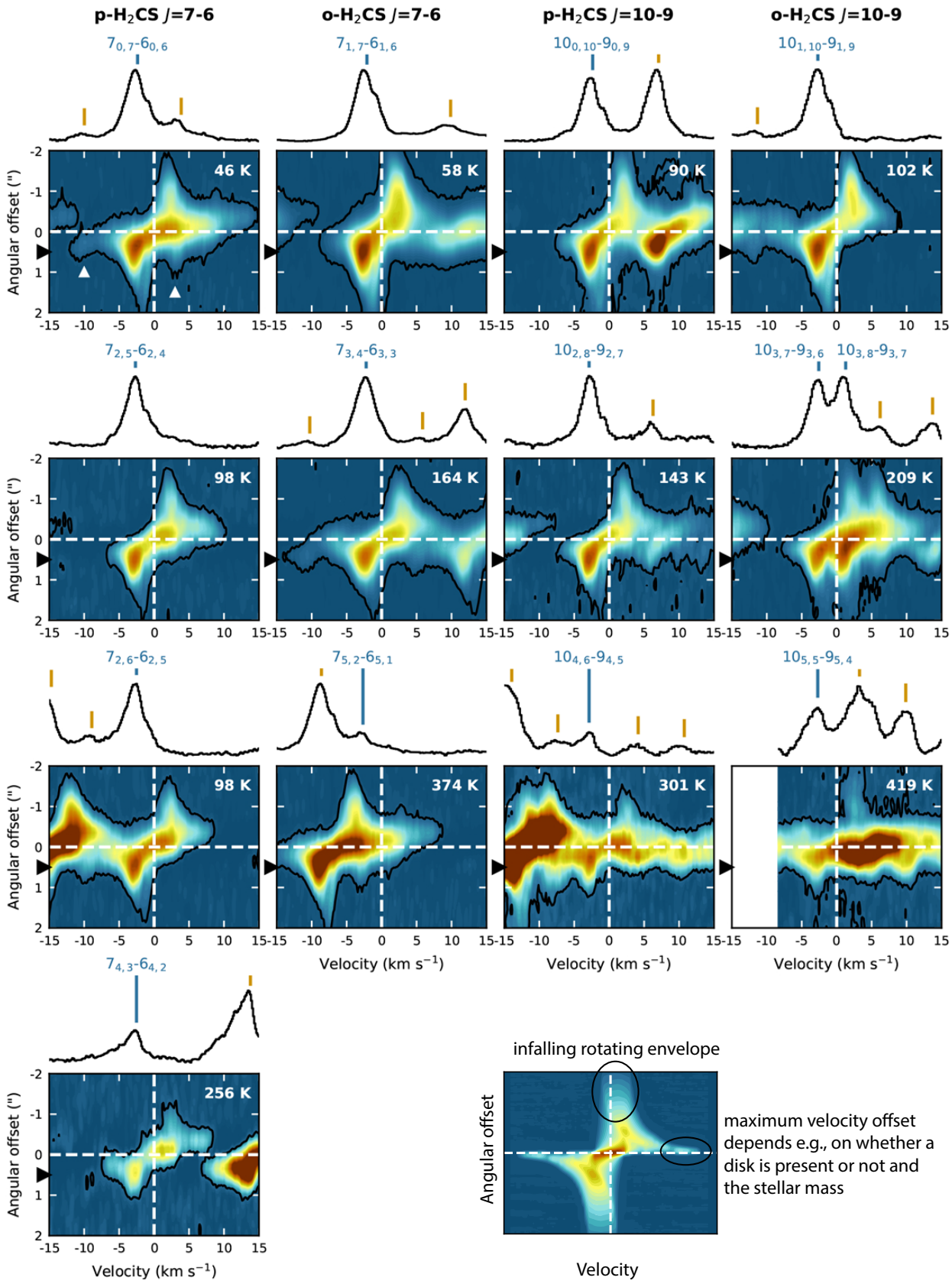

Fig. 3. Position–velocity diagrams of the H_2CS lines along the major axis (PA = 65°) of the disk-like structure (positive angular offsets denote the northeast direction, i.e., blueshifted emission, negative offsets denote the southwest direction, i.e., redshifted emission). The intensity (color) scale is normalized to the brightest line in each panel. The black contour denotes the 3σ contour. The dashed white lines give the source position and systemic velocity of 3.8 km s^{-1} (shifted to 0 km s^{-1}). The upper level energy is denoted in the top right corner of each panel. The spectra at ~0.5″ northeast of the source (indicated by black triangles left of the vertical axes) are superimposed on the pv diagram panels. The H_2CS lines are identified by a vertical blue line, other lines by vertical orange lines. The white triangles in the *top left panel* highlight blending of the $7_{0,7}$–$6_{0,6}$ line. For reference, *bottom right panel*: pv diagram for a thin-disk model with Keplerian disk and infalling rotating envelope.

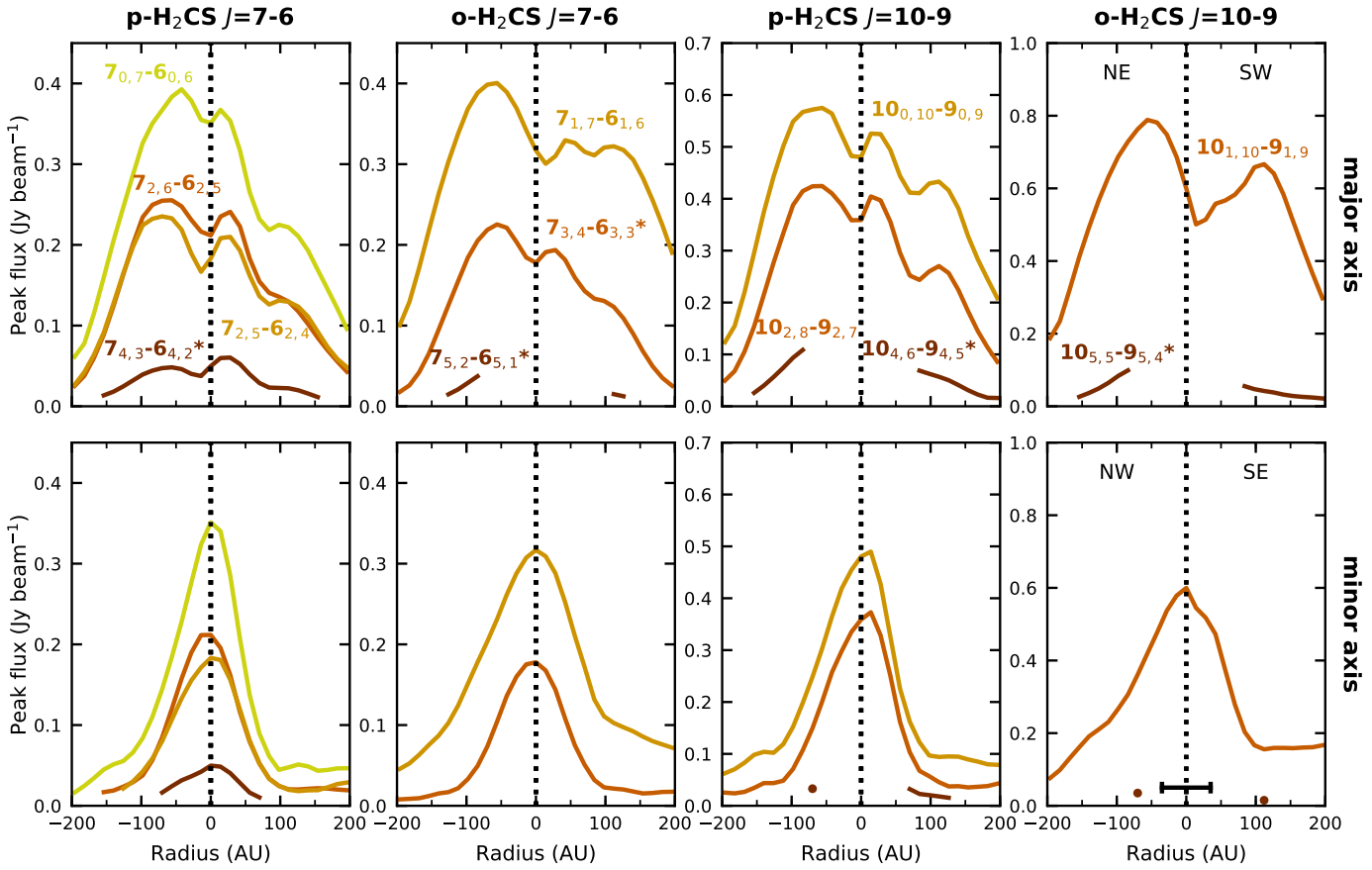

Fig. 4. Radial profiles of the H_2CS peak fluxes along the major axis (PA = 45°; *top panels*) and minor axis (PA = 135°; *bottom panels*) of the disk-like structure. In each panel, transitions with higher upper level energy are plotted in darker colors. Fluxes for transitions labeled with an asterisk (∗) have been divided by 2 to account for two transitions with the same upper level energy and Einstein A coefficent at the same frequency (see Table A.1). The horizontal bar in the *lower right panel* marks the beam size. The rms ranges between 2 and 8 mJy beam^{-1}.

centrifugal barrier (at ∼50 AU). However, careful analysis of the data shows that a weak line is present on both the blue and red side of this H_2CS line (see Fig. 3, top left panel). The large velocity gradient thus seems to be the result of line blending and not Keplerian rotation. This conclusion is reinforced by the velocity structure of the other H_2CS lines. The unblended $7_{2,5}$–$6_{2,4}$ line shows a maximum velocity offset of ∼6 km s^{-1} on the blue side, and ∼10 km s^{-1} on the red side. Unblended wings from the other lines show similar offsets. The unblended H_2CS velocity offsets are comparable to those for OCS J = 19−18 (Oya et al. 2016), except for OCS the offset is ∼8 km s^{-1} on the red side and ∼10 km s^{-1} on the blue side. Oya et al. (2016) showed that the OCS emission cannot be explained by Keplerian motions, but requires both rotation and infall. A Keplerian component in the inner part of the rotating-infalling disk-like structure thus cannot be established with the current observations.

3.2. Peak fluxes

Most lines show some degree of blending, such that generally, in the central pixels (∼0.5″ radius), one or both of the line wings overlap with the wing of another line. As this does not significantly influence the peak flux, we extract the peak flux per pixel in order to make spatial maps of the line ratios and hence temperature structure. Pixels with too much line blending to extract a reliable peak flux are excluded. Since the data cover only one ortho-H_2CO and one para-H_2CO line, the main isotopologue lines cannot be used for a temperature measurement and we exclude H_2CO from further analysis. The D_2CO $6_{4,2}$–$5_{4,1}$ and $6_{4,3}$–$5_{4,2}$ lines, as well as the H_2CS $10_{3,7}$–$9_{3,6}$ and $10_{3,8}$–$9_{3,7}$ lines, are located within 4 MHz of each other and are too blended to obtain individual peak fluxes (see also Figs. 3 and B.3). Maps of the peak fluxes (moment 8 maps) of the remaining $H_2^{13}CO$, D_2CO and H_2CS lines without severe blending are presented in Appendix C and radial profiles for the H_2CS lines are shown in Fig. 4.

All H_2CS lines show an elongated structure with the major axis at ∼45° (Figs. 2 and C.1). This is slightly different from the 65°±10° derived by Oya et al. (2016), but radial profiles along a position angle of 45° or 65° are very similar. For all lines, the emission peaks on either side of the continuum peak, as has been seen for most other species toward IRAS 16293A (see, e.g., Calcutt et al. 2018; Manigand et al. 2019). This could correspond to the double peaks seen in centimeter continuum emission (Wootten 1989; Chandler et al. 2005; Pech et al. 2010), although those positions are slightly off (see discussion in Calcutt et al. 2018). Alternatively, they can be due to an edge-on rotating toroidal structure, as seen, for example, in synthetic CO images (Jacobsen et al. 2018). The NE peak is ∼60 AU offset from the continuum peak, except for the $7_{0,7}$–$6_{0,6}$ transition that peaks around ∼40 AU (see Fig. 4). The SW peak is around ∼25 AU, and is weaker than the NE peak, except for the $7_{4,3}$–$6_{4,2}$ transition. Most H_2CS lines seem to have a weaker third peak ∼120 AU SW off the source center. The $H_2^{13}CO$ and D_2CO lines also show an elongated double-peaked structure, albeit more compact and without the third peak seen for H_2CS (Fig. C.2). In addition, the

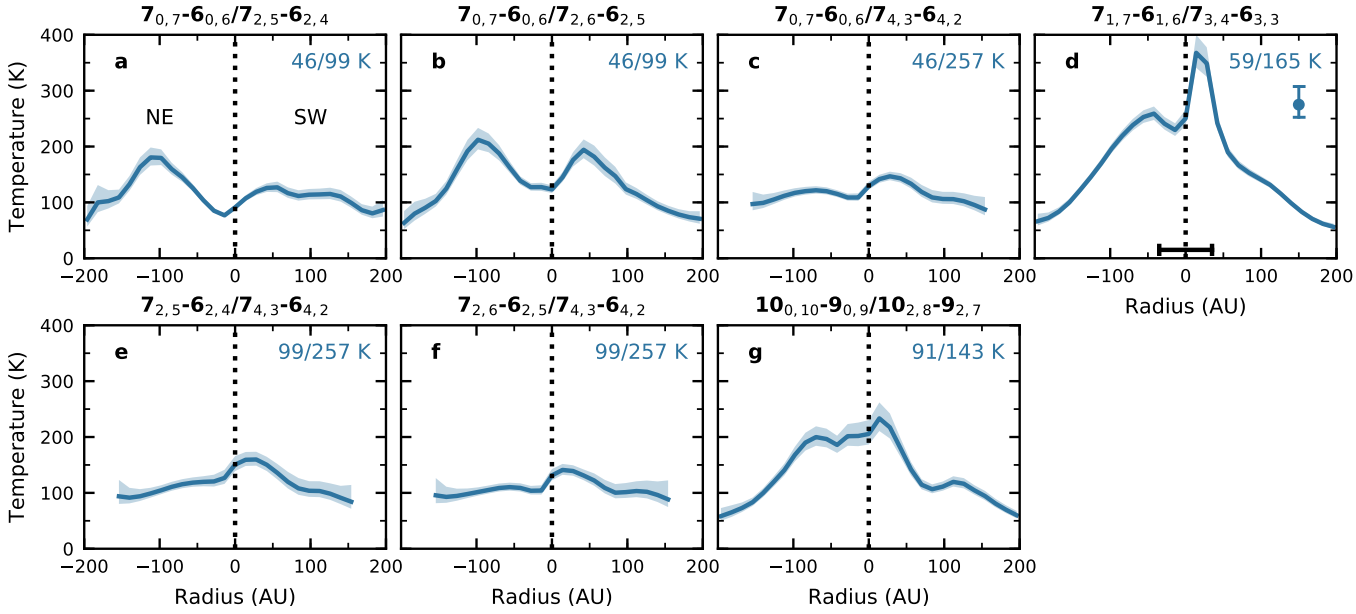

Fig. 5. Radial temperature profiles derived from H_2CS line ratios (listed above the panels) along the major axis of the disk-like structure (PA = 45°) using the RADEX results. The upper level energies of the transitions are listed in the top right corner of each panel. The shaded area represents the 1σ uncertainty based on the noise level of the observations. The vertical bar in the *top right panel* shows a 3σ error bar representative for the inner 100 AU and the horizontal bar marks the beam size.

northern part is more elongated perpendicular to the major axis than for the H_2CS lines.

3.3. Temperature

Only H_2CS lines are used in the temperature analysis, for the reasons outlined below. For $H_2^{13}CO$ there are three line ratios that probe temperature ($5_{0,5}$–$4_{0,4}$/$5_{2,4}$–$4_{2,3}$, $5_{0,5}$–$4_{0,4}$/$5_{4,1}$–$4_{4,0}$, and $5_{2,4}$–$4_{2,3}$/$5_{4,1}$–$4_{4,0}$), but for the two highest energy lines, the continuum seems to be oversubtracted to varying degrees in different pixels. Reliable peak fluxes can therefore not be obtained for these two lines, leaving only a single suitable $H_2^{13}CO$ line, and therefore $H_2^{13}CO$ is not used to derive the temperature structure. For D_2CO there are six suitable line ratios. However, all these ratios are near unity, suggesting that the emission is optically thick (see Appendix C). Their brightness temperature is ~30 K, much lower than expected for the inner region of an envelope, as also shown for other optically thick lines in the PILS data (e.g., CH_2DOH; Jørgensen et al. 2018), indicating that those lines probe colder foreground material.

The maps of the H_2CS peak fluxes are used to calculate line ratios, and these are converted into temperature maps using a grid of RADEX non-local thermodynamic equilibrium (non-LTE) radiative transfer models (van der Tak et al. 2007). The molecular data are obtained from the Leiden Atomic and Molecular Database (LAMDA; Schöier et al. 2005, which contains collisional rate coefficients for H_2CS from Wiesenfeld & Faure 2013). The line ratios as a function of temperature for different H_2 densities and H_2CS column densities are shown in Fig. D.1. For densities $\gtrsim 10^6$–10^7 cm^{-3} and column densities $\lesssim 10^{15}$ cm^{-2} the line ratios are independent of density and column density, respectively, and are thus good tracers of the temperature. For a disk-like structure, densities are expected to be $>10^7$ cm^{-3}, so the exact value adopted for the density does not influence the derived temperatures and we use a value of 10^{10} cm^{-3}. Toward IRAS 16293B, a H_2CS column density of 1.3×10^{15} cm^{-2} was found (Drozdovskaya et al. 2018). As is discussed later in this section, based on the line ratios, the H_2CS column density toward IRAS 16293A cannot exceed more than a few times 10^{15} cm^{-2}. A column density of 10^{14} cm^{-2} is adopted in the temperature calculations. All H_2CS lines are optically thin at this column density. At a column of 10^{15} cm^{-2}, the $7_{1,7}$–$6_{1,6}$ and $10_{1,10}$–$9_{1,9}$ transitions become optically thick (see Fig. D.2), lowering the derived temperature by $\lesssim$10 K (see Fig. D.1). In addition to a density and column density, a line width of 2 km s^{-1} is adopted to convert the observed line ratios to temperature. Error bars on the line ratios are calculated from the image rms, and converted into error bars on the temperature using the RADEX calculations (see Fig. D.1). The error bars therefore depend on the sensitivity of the line ratio to the temperature and the relative uncertainty on the peak flux. Since collisional rate coefficients are not available for all observed transitions, we also performed LTE calculations.

Radial temperature profiles along the major axis of the disk-like structure (PA = 45°) are presented in Fig. 5 for ratios with collisional rate coefficients and in Fig. E.1 for the remaining ratios. Figure E.2 shows radial temperature profiles for different position angles. For clarity, we refer to the panels in Fig. 5 instead of to the quantum numbers of the line ratios in the following discussion. Along the major axis, all line ratios result in temperatures between ~100 and ~175 K out to ~150 AU, with temperatures dropping to ~75 K at ~200 AU. The non-LTE RADEX results give temperatures higher by ~20–50 K than the LTE results (see Fig. E.1), suggesting that the lines are not completely thermalized. Panels d and g show temperatures $\gtrsim$150 K in the inner ~100 AU. On the other hand, panels a and b display a decrease in temperature in the inner ~100 AU (down to ~100 K). The other three p-H_2CS ratios (panels c, e and f) show a rather flat temperature profile, with temperatures of ~100–150 K throughout the inner 150 AU. The five line ratios in Fig. E.1 cannot be used to constrain the temperature in the inner 100 AU due to severe line blending, but the temperature between ~100–150 AU is >100 K. Another constraint can be provided by the ratio between the different ΔJ transitions. The 10–9 lines are

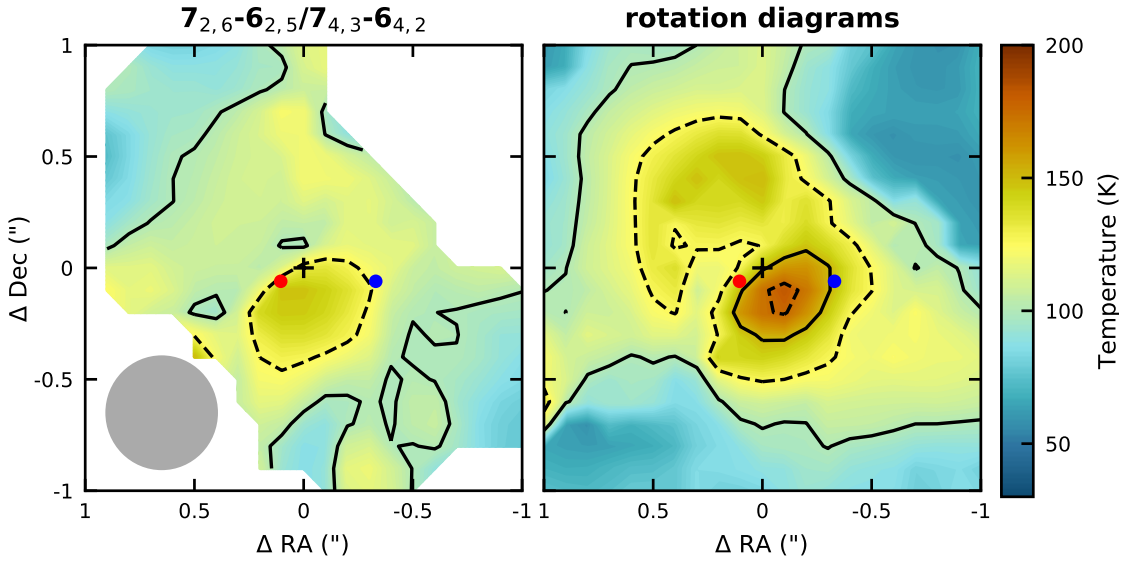

Fig. 6. Temperature in a 2″ × 2″ (280 × 280 AU) region around IRAS 16293A derived from the H_2CS $7_{2,6}$–$6_{2,5}$/$7_{4,3}$–$6_{4,2}$ line ratio (*left panel*), and from the rotation diagrams in each pixel (*right panel*). Solid contours indicate temperatures of 100 and 150 K and dashed contours are at 125 and 175 K. The continuum peak position is marked with a black cross. The positions of the unresolved binary components A1 and A2 in 2015 (Hernández-Gómez et al. 2019) are shown with a red and blue circle, resp. The beam is depicted in the lower left corner of the *left panel*.

brighter than the 7−6 lines over the 200 AU radius studied, which means temperatures ≳60 K (see Fig. D.1).

The central decrease in panels a and b is not likely to be due to the continuum becoming optically thick because a similar effect would then be expected in panels c, e, and f. Instead, it could be due to the fact that the $7_{0,7}$–$6_{0,6}$ line (which has the lowest upper level energy) peaks closer to the continuum position than the other lines, causing a central increase in the line ratio, and hence a decrease in the derived temperature. In addition, the temperature derived from these ratios is very sensitive to small changes in the fluxes because the energy levels involved range from only 46 to 98 K (see Fig. D.1). The ratio changes from 1.4 to 1.5 if the temperature drops from 200 to 150 K, and to 1.8 at 100 K. This means that a variation of <10% in one of the peak fluxes can change the derived temperature from 200 to 150 K, and a 20% variation can change the temperature from 150 to 100 K. These variations can occur even though the transitions are present in the same dataset, as can be seen from the difference between panels a and b (and Fig. 4, upper left panel). The $7_{2,6}$–$6_{2,5}$ and $7_{2,5}$–$6_{2,4}$ transitions have the same upper level energy and Einstein A coefficient, and should thus be equally strong. However, in the SW there is a 100 K difference in the derived temperature using either of the two lines. This variation is slightly larger than the 3σ uncertainty based on the rms noise, and may be due to blending with a weak line.

The $7_{4,3}$–$6_{4,2}$ has a relatively high upper level energy (257 K), and therefore temperatures derived using this transition are less sensitive to flux changes. For example, as the temperature increases from 100 to 200 K, the $7_{0,7}$–$6_{0,6}$/$7_{4,3}$–$6_{4,2}$ ratio decreases from 11 to 4.1, and the $7_{2,6}$–$6_{2,5}$/$7_{4,3}$–$6_{4,2}$ ratio decreases from 6.1 to 2.9. A temperature map for the 2″ × 2″ region around IRAS 16293A derived from the $7_{2,6}$–$6_{2,5}$/$7_{4,3}$–$6_{4,2}$ ratio (panel f) is presented in Fig. 6. The positions of the unresolved binary components of the A source, A1 and A2, are indicated as well. A1 and A2 have been observed to move relative to each other (e.g., Loinard 2002) with a global southwest movement. Since the observations used here were performed between 2014 and 2016, we plot the positions A1 and A2 had in 2015 (Hernández-Gómez et al. 2019). Figure 6 shows that the radial temperature profiles are not strongly affected by the chosen position angle or the binary components.

The higher temperatures in panels d and g are likely due to optical depth effects. As can be seen from Fig. D.2, the $7_{1,7}$–$6_{1,6}$ and $10_{0,10}$–$9_{0,9}$ transitions are among the first transitions to become optically thick. If these transitions are optically thick while the higher energy transitions remain optically thin, the flux of the lower energy transition is too low, and hence the derived temperature is too high. In turn, an estimate of the H_2CS column density can be made based on these results; for the $7_{0,7}$–$6_{0,6}$ transition to remain optically thin, the column density of para H_2CS cannot exceed more than a few times 10^{15} cm^{-2}.

To assess whether one of the H_2CS lines is affected by blending with a weak line at a similar frequency and therefore has its peak flux overestimated, rotation diagrams are made for every pixel in a 2″ × 2″ region surrounding the continuum position. Representative diagrams at 0.5″ and 1.0″ offsets are presented in Fig. 7. An ortho-to-para ratio of 2 is assumed, but varying this between 1 and 3 changes the derived temperature by ≲30 K. At offsets ≳0.8″ all transitions follow a straight line, and similar temperatures are found when using all transitions, only ortho transitions, or only para transitions in the fit. At smaller angular offsets the scatter becomes larger, but no transition is found to strongly deviate from the general trend. For the lower energy transitions (E_{up} < 200 K) this scatter is at least partly the result of some of the transitions becoming optically thick.

Radial profiles based on the temperatures derived from the rotation diagrams are shown in Fig. 8. These profiles are constructed from fitting either all transitions, only transitions with E_{up} < 200 K, only para transitions, or only ortho transitions. The first three cases result in temperatures of ~60 K at 200 AU increasing to ~150 at source center. Using only the ortho transitions results in temperatures >200 K in the inner 100 AU, likely because the lower energy transitions become optically thick. The central decrease in temperature seen for the $7_{0,7}$–$6_{0,6}$/$7_{2,5}$–$6_{2,4}$ and $7_{0,7}$–$6_{0,6}$/$7_{2,6}$–$6_{2,5}$ ratios (panels a and b in Fig. 5) is not seen in these profiles, and may be due to the $7_{0,7}$–$6_{0,6}$

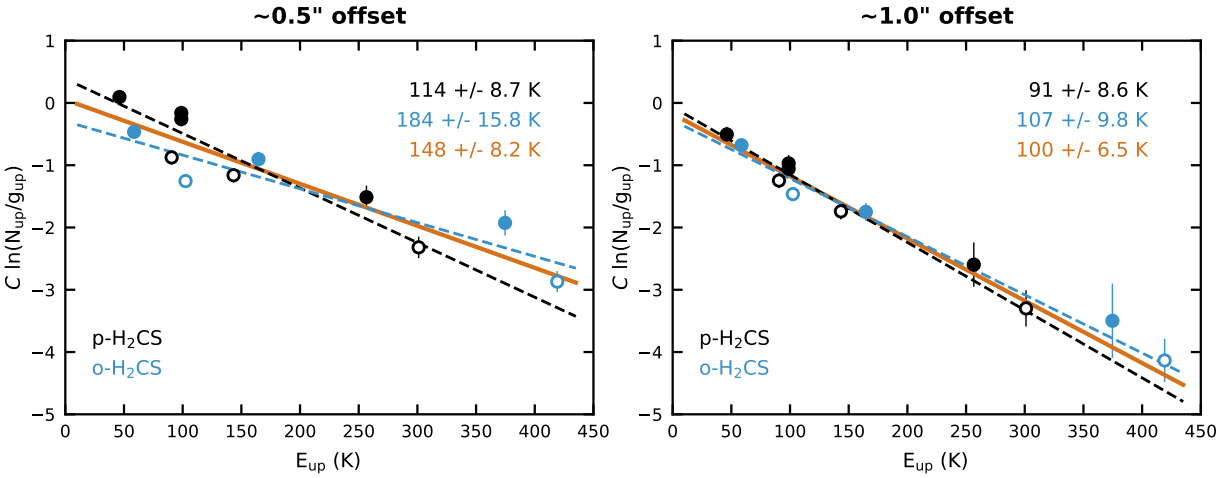

Fig. 7. Rotation diagrams for the H_2CS peak fluxes along the major axis (PA = 45°) of the disk-like structure at 0.5″ (*left panel*) and 1.0″ (*right panel*) from the source center. Para transitions are shown in black and ortho transitions in blue. An ortho-to-para ratio of 2 is assumed. J = 7–6 transitions are displayed as filled symbols and J = 10–9 transitions as open symbols. The error bars include a 10% uncertainty. The best fit to all transitions is presented by the solid orange line, whereas the dashed lines show fits to only the ortho (blue) and only the para transitions (black). The corresponding rotation temperatures are listed in the top right corners.

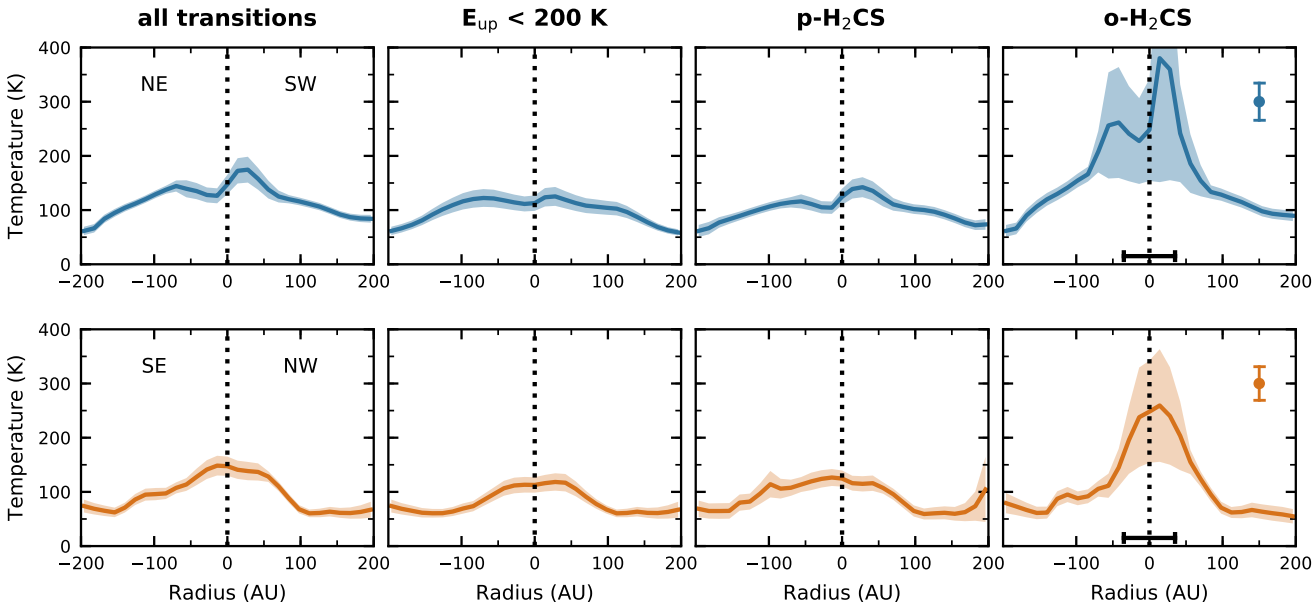

Fig. 8. Radial temperature profiles derived from the rotation diagrams including all transitions (*first column*), only transitions with E_{up} < 200 K (*second column*), only para transitions (*third column*), or only ortho transitions (*fourth column*). *Top row*: radial profiles along the major axis of the disk-like structure (PA = 45°), *bottom row*: profiles along the minor axis. The shaded area represents the 1σ uncertainty. The vertical bar in the *right panels* shows a typical 3σ error for the inner 100 AU and the horizontal bar marks the beam size.

transition peaking closer in and these ratios being not sensitive to temperature, as discussed above.

4. Discussion

Based on line ratios of several J = 7–6 and J = 10–9 H_2CS transitions, the temperature in the inner ~150 AU of IRAS 16293A is ~100–175 K, and drops to ~75 K at ~200 AU. In Fig. 9 the H_2CS temperature profiles are compared to temperature profiles obtained from continuum radiative transfer modeling and from spatially unresolved H_2O observations with the ISO satellite (Ceccarelli et al. 2000; Schöier et al. 2002; Crimier et al. 2010). These latter profiles were derived assuming a spherically symmetric collapsing envelope structure around a single protostar. Recently, Jacobsen et al. (2018) performed detailed 3D radiative transfer modeling including two protostars. All previously derived temperatures show a very similar structure with a radial power law dependence of approximately $T \propto r^{-0.7}$ in the inner few hundred AU and a temperature of 100 K around ~100 AU. The H_2CS temperature is consistent with the envelope temperature profiles down to radii of ~100 AU, but lacks the temperature rise at smaller radii.

Such a flattening of the temperature could be the result of efficient cooling by water molecules that are released into the gas phase at ~100 K. However, water can also heat the gas through absorption of near-IR photons from warm dust. Ceccarelli et al. (1996) studied the gas and dust temperature profile of an infalling envelope with a model that includes dynamics, chemistry, and

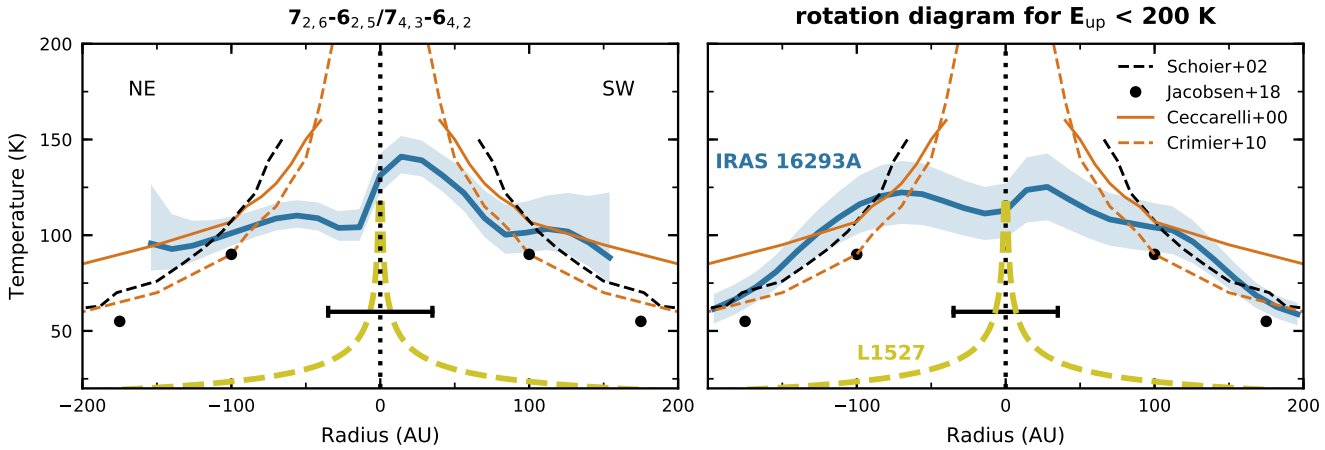

Fig. 9. Radial temperature profiles for IRAS 16293A derived in this work from H_2CS transitions (blue lines) compared to dust (black lines and circles) and gas (orange lines) temperature profiles from the literature. The H_2CS temperature profile in the *left panel* is derived from the $7_{2,6}$–$6_{2,5}$/$7_{4,3}$–$6_{4,2}$ line ratio and the profile in the *right panel* is based on fits to the peak flux rotation diagrams including only transitions with E_{up} < 200 K. The blue shaded area represents the 1σ uncertainty. The dashed black line shows the IRAS 16293 dust temperature assuming an envelope around a central source of 27 $L_\odot$ (Schöier et al. 2002), and the black dots represents dust temperature contours for IRAS 16293A from detailed modeling including both protostars and the bridge structure (Jacobsen et al. 2018). The gas temperatures are based on H_2O observations with the ISO satellite using a model that computes the gas temperature through an envelope by solving a chemical network and equating the heating and cooling rates (Ceccarelli et al. 1996). The solid orange line shows the initial results assuming a single 27 $L_\odot$ protostar at 160 pc (Ceccarelli et al. 2000), the dashed orange line presents the revised results for a 22 $L_\odot$ protostar at 120 pc (Crimier et al. 2010). The dashed yellow line shows the midplane gas temperature for the Class 0/I disk L1527 based on optically thick ^{13}CO and $C^{18}O$ emission (van 't Hoff et al. 2018). The horizontal bar marks the beam size of the H_2CS observations.

heating and cooling, and concluded that the gas and dust temperatures are generally well coupled. For different model parameters (e.g., luminosity, mass accretion rate, stellar mass) the difference between the gas and dust temperature ranges from ~10 K to more than a 100 K, but applying this model to IRAS 16293 (assuming a collapsing envelope around a single central source of 27 $L_\odot$) results in differences of only a few Kelvin between the gas and dust (Ceccarelli et al. 2000; Crimier et al. 2010). However, this model does not include a disk or disk-like structure. The presence of a disk may result in lower temperatures than in the case of only an envelope, as for example shown by the models from Whitney et al. (2003), observations toward VLA 1623 (Murillo et al. 2015), and analysis of $H_2^{18}O$ observations toward four protostars in Perseus (Persson et al. 2016).

A chemical depletion of H_2CS in the inner region is not likely to cause a flat instead of increasing temperature profile because the line ratios are independent of abundance. The dust opacity could play a role in veiling the hottest inner region, but no absorption is observed, as expected for colder gas in front of warmer dust. However, the situation is likely complicated with the dust and strongest lines being only marginally optically thick on scales of the beam, but much thicker on smaller unresolved scales. This may lead to quenching of the higher excitation lines, while the emission from the lower excitation lines is only slightly reduced, and therefore results in a lower derived excitation temperature. On the other hand, this effect may be mitigated by the fact that multiple lines of sight are integrated in the beam. Detailed radiative transfer modeling is thus required to properly constrain the influence of the dust.

Figure 9 also shows the gas temperature profile for the embedded Class 0/I disk L1527 based on optically thick ^{13}CO and $C^{18}O$ observations (van 't Hoff et al. 2018), illustrating that the temperature in the disk is ~75 K lower than in the IRAS 16293A disk-like structure. This is consistent with the higher accretion rate and higher luminosity of IRAS 16293A (~4×10^{-6}–$5 \times 10^{-5} M_\odot$ yr^{-1} and 18 $L_\odot$; Schöier et al. 2002; Jacobsen et al. 2018) compared to L1527 ($3 \times 10^{-7} M_\odot$ yr^{-1} and 1.9–2.6 $L_\odot$; Kristensen et al. 2012; Tobin et al. 2012, 2013). As the accretion rate drops in the late stages of the evolution of embedded protostar, this suggests that the temperature of the disk or disk-like structure drops accordingly.

Oya et al. (2016) also used the $7_{0,7}$–$6_{0,6}$/$7_{2,5}$–$6_{2,4}$ and $7_{0,7}$–$6_{0,6}$/$7_{4,3}$–$6_{4,2}$ ratios (Fig. 5, panels a and c) to measure the gas temperature in the envelope, disk and envelope-disk interface (centrifugal barrier). Using the flux within a 0.5″ region at 0″, 0.5″ (70 AU) and 1.0″ (140 AU) offsets from the continuum peak position along the disk major axis (PA = 65°) integrated over different velocity ranges at each position, they derive temperatures between 70 and 190 K. In addition, they find the highest temperatures at the 0.5″ offset position and attribute these temperature increases to weak accretion shocks at the centrifugal barrier (~50 AU) or to directly heating of a more extended envelope in front of the centrifugal barrier. Although we find a similar temperature range for the inner ~150 AU, we do not see temperature peaks in the $7_{0,7}$–$6_{0,6}$/$7_{4,3}$–$6_{4,2}$ (Fig. 5, panel c). Peaks are visible for the $7_{0,7}$–$6_{0,6}$/$7_{2,5}$–$6_{2,4}$ and $7_{0,7}$–$6_{0,6}$/$7_{2,6}$–$6_{2,5}$ (Fig. 5, panels a and b), but this is likely due to the $7_{0,7}$–$6_{0,6}$ transition peaking slightly closer to the protostar than the other transitions in combination with the high sensitivity of these ratios to small changes in flux, as discussed in Sect. 3.3. Moreover, no temperature peaks are found from the $7_{2,5}$–$6_{2,4}$/$7_{4,3}$–$6_{4,2}$ and $7_{2,6}$–$6_{2,5}$/$7_{4,3}$–$6_{4,2}$ ratios (Fig. 5, panels e and f) or from the rotational diagrams. Additional higher resolution observations thus seem necessary to substantiate local temperature enhancements at the centrifugal barrier.

5. Conclusions

We used H_2CS line ratios observed in the ALMA-PILS survey to study the gas temperature in the disk-like structure around the Class 0 protostar IRAS 16293A. Because of the line-richness of

this source, almost all H_2CS lines are blended in their line wings. Therefore, peak fluxes extracted per pixel are used in the analysis instead of integrated fluxes. Formaldehyde is not used because the optically thick H_2CO and D_2CO lines also trace colder foreground material, and not enough unblended $H_2^{13}CO$ transitions were available. Our conclusions can be summarized as follows:

- Strong evidence for a rotationally supported disk is still lacking: the high-velocity wings of the H_2CS $7_{0,7}$–$6_{0,6}$ transition are the result of blending with nearby weak lines instead of a Keplerian disk.
- The temperature is between ∼100 and 175 K in the inner ∼150 AU, and drops to ∼75 K at ∼200 AU. This profile is consistent with envelope temperature profiles constrained on 1000 AU scales down to scales of ∼100 AU ($T \propto r^{-0.7}$ in the region where the dust becomes optically thick). However, the envelope profile breaks down in the inner most region that can now be probed by ALMA because the observed temperature does not show a steep rise at radii $\lesssim$100 AU.
- The temperature in the disk-like structure around IRAS 16293A is ∼75 K higher than in the young Class 0/I disk L1527, on similar scales.

The flattening of the temperature profile at radii $\lesssim$100 AU may be the result of efficient cooling by water that has sublimated from the grains in this region. Alternatively, the presence of a disk could affect the temperature structure by having a larger fraction of the mass at higher density and lower temperatures. High-resolution observations of optically thin lines are required to establish the details of the temperature profile in the inner ∼100 AU.

Acknowledgements. We would like to thank the referee for a prompt and positive report and Yuri Aikawa, Karin Öberg, Jonathan Williams and Niels Ligterink for comments on the manuscript. Astrochemistry in Leiden is supported by the Netherlands Research School for Astronomy (NOVA). M.L.R.H acknowledges support from a Huygens fellowship from Leiden University. The research of J.K.J is supported by the European Union through the ERC Consolidator Grant "S4F" (grant agreement No 646908). This paper makes use of the following ALMA data: ADS/JAO.ALMA#2012.1.00712.S, ADS/JAO.ALMA#2013.1.00278.S and ADS/JAO.ALMA#2016.1.01150.S. ALMA is a partnership of ESO (representing its member states), NSF (USA) and NINS (Japan), together with NRC (Canada), MOST and ASIAA (Taiwan), and KASI (Republic of Korea), in cooperation with the Republic of Chile. The Joint ALMA Observatory is operated by ESO, AUI/NRAO and NAOJ.

References

Andrews, S. M., & Williams, J. P. 2005, ApJ, 631, 1134
Ansdell, M., Williams, J. P., van der Marel, N., et al. 2016, ApJ, 828, 46
Bocquet, R., Demaison, J., Poteau, L., et al. 1996, J. Mol. Spectr., 177, 154
Bocquet, R., Demaison, J., Cosléou, J., et al. 1999, J. Mol. Spectr., 195, 345
Boley, A. C. 2009, ApJ, 695, L53
Boss, A. P. 1997, Science, 276, 1836
Bottinelli, S., Ceccarelli, C., Neri, R., et al. 2004, ApJ, 617, L69
Brünken, S., Müller, H. S. P., Lewen, F., & Winnewisser, G. 2003, Phys. Chem. Chem. Phys., 5, 1515
Calcutt, H., Jørgensen, J. K., Müller, H. S. P., et al. 2018, A&A, 616, A90
Cassen, P., & Moosman, A. 1981, Icarus, 48, 353
Caux, E., Kahane, C., Castets, A., et al. 2011, A&A, 532, A23
Cazaux, S., Tielens, A. G. G. M., Ceccarelli, C., et al. 2003, ApJ, 593, L51
Ceccarelli, C., Hollenbach, D. J., & Tielens, A. G. G. M. 1996, ApJ, 471, 400
Ceccarelli, C., Castets, A., Caux, E., et al. 2000, A&A, 355, 1129
Chandler, C. J., Brogan, C. L., Shirley, Y. L., & Loinard, L. 2005, ApJ, 632, 371
Codella, C., Cabrit, S., Gueth, F., et al. 2014, A&A, 568, L5
Cornet, R. A., & Winnewisser, G. 1980, J. Mol. Spectr., 80, 438
Crimier, N., Ceccarelli, C., Maret, S., et al. 2010, A&A, 519, A65
Dangoisse, D., Willemot, E., & Bellet, J. 1978, J. Mol. Spectr., 71, 414
Drozdovskaya, M. N., van Dishoeck, E. F., Jørgensen, J. K., et al. 2018, MNRAS, 476, 4949
Dutrey, A., Guilloteau, S., Piétu, V., et al. 2017, A&A, 607, A130
Dzib, S. A., Ortiz-León, G. N., Hernández-Gómez, A., et al. 2018, A&A, 614, A20
Fabricant, B., Krieger, D., & Muenter, J. S. 1977, J. Chem. Phys., 67, 1576
Favre, C., Jørgensen, J. K., Field, D., et al. 2014, ApJ, 790, 55
Foster, J. B., Mandel, K. S., Pineda, J. E., et al. 2013, MNRAS, 428, 1606
Harsono, D., Bruderer, S., & van Dishoeck, E. F. 2015, A&A, 582, A41
Harsono, D., Bjerkeli, P., van der Wiel, M. H. D., et al. 2018, Nat. Astron., 2, 646
Hernández-Gómez, A., Loinard, L., Chandler, C. J., et al. 2019, ApJ, 875, 94
Jacobsen, S. K., Jørgensen, J. K., van der Wiel, M. H. D., et al. 2018, A&A, 612, A72
Jørgensen, J. K., van Dishoeck, E. F., Visser, R., et al. 2009, A&A, 507, 861
Jørgensen, J. K., van der Wiel, M. H. D., Coutens, A., et al. 2016, A&A, 595, A117
Jørgensen, J. K., Müller, H. S. P., Calcutt, H., et al. 2018, A&A, 620, A170
Kristensen, L. E., van Dishoeck, E. F., Bergin, E. A., et al. 2012, A&A, 542, A8
Kwon, W., Looney, L. W., Mundy, L. G., Chiang, H.-F., & Kemball, A. J. 2009, ApJ, 696, 841
Li, Z.-Y., Banerjee, R., Pudritz, R. E., et al. 2014, Protostars and Planets VI (Tucson, AZ: University of Arizona Press), 173
Lindberg, J. E., Jørgensen, J. K., Brinch, C., et al. 2014, A&A, 566, A74
Loinard, L. 2002, Rev. Mex. Astron. Astrofis., 38, 61
Looney, L. W., Mundy, L. G., & Welch, W. J. 2000, ApJ, 529, 477
Maeda, A., Medvedev, I. R., Winnewisser, M., et al. 2008, ApJS, 176, 543
Manara, C. F., Morbidelli, A., & Guillot, T. 2018, A&A, 618, L3
Mangum, J. G., & Wootten, A. 1993, ApJS, 89, 123
Manigand, S., Calcutt, H., Jørgensen, J. K., et al. 2019, A&A, 623, A69
Miotello, A., Testi, L., Lodato, G., et al. 2014, A&A, 567, A32
Müller, H. S. P., & Lewen, F. 2017, J. Mol. Spectr., 331, 28
Müller, H. S. P., Gendriesch, R., Margulès, L., et al. 2000, Phys. Chem. Chem. Phys., 2, 3401
Müller, H. S. P., Thorwirth, S., Roth, D. A., & Winnewisser, G. 2001, A&A, 370, L49
Müller, H. S. P., Schlöder, F., Stutzki, J., & Winnewisser, G. 2005, J. Mol. Struct., 742, 215
Müller, H. S. P., Maeda, A., Thorwirth, S., et al. 2019, A&A, 621, A143
Mundy, L. G., Wootten, A., Wilking, B. A., Blake, G. A., & Sargent, A. I. 1992, ApJ, 385, 306
Murillo, N. M., Lai, S.-P., Bruderer, S., Harsono, D., & van Dishoeck, E. F. 2013, A&A, 560, A103
Murillo, N. M., Bruderer, S., van Dishoeck, E. F., et al. 2015, A&A, 579, A114
Öberg, K. I., Murray-Clay, R., & Bergin, E. A. 2011, ApJ, 743, L16
Öberg, K. I., Furuya, K., Loomis, R., et al. 2015, ApJ, 810, 112
Oya, Y., Sakai, N., López-Sepulcre, A., et al. 2016, ApJ, 824, 88
Pagani, L., Steinacker, J., Bacmann, A., Stutz, A., & Henning, T. 2010, Science, 329, 1622
Pech, G., Loinard, L., Chandler, C. J., et al. 2010, ApJ, 712, 1403
Persson, M. V., Harsono, D., Tobin, J. J., et al. 2016, A&A, 590, A33
Persson, M. V., Jørgensen, J. K., Müller, H. S. P., et al. 2018, A&A, 610, A54
Pineda, J. E., Maury, A. J., Fuller, G. A., et al. 2012, A&A, 544, L7
Qi, C., Öberg, K. I., Wilner, D. J., et al. 2013, Science, 341, 630
Qi, C., Öberg, K. I., Andrews, S. M., et al. 2015, ApJ, 813, 128
Qi, C., Öberg, K. I., Espaillat, C. C., et al. 2019, ApJ, 882, 160
Sakai, N., Sakai, T., Hirota, T., et al. 2014, Nature, 507, 78
Schöier, F. L., Jørgensen, J. K., van Dishoeck, E. F., & Blake, G. A. 2002, A&A, 390, 1001
Schöier, F. L., Jørgensen, J. K., van Dishoeck, E. F., & Blake, G. A. 2004, A&A, 418, 185
Schöier, F. L., van der Tak, F. F. S., van Dishoeck, E. F., & Black, J. H. 2005, A&A, 432, 369
Taquet, V., van Dishoeck, E. F., Swayne, M., et al. 2018, A&A, 618, A11
Tobin, J. J., Hartmann, L., Chiang, H.-F., et al. 2012, Nature, 492, 83
Tobin, J. J., Hartmann, L., Chiang, H.-F., et al. 2013, ApJ, 771, 48
Tobin, J. J., Looney, L. W., Li, Z.-Y., et al. 2016, ApJ, 818, 73
Tychoniec, Ł., Tobin, J. J., Karska, A., et al. 2018, ApJS, 238, 19
van der Tak, F. F. S., Black, J. H., Schöier, F. L., Jansen, D. J., & van Dishoeck, E. F. 2007, A&A, 468, 627
van Dishoeck, E. F., Jansen, D. J., & Phillips, T. G. 1993, A&A, 279, 541
van Dishoeck, E. F., Blake, G. A., Jansen, D. J., & Groesbeck, T. D. 1995, ApJ, 447, 760
van 't Hoff, M. L. R., Tobin, J. J., Harsono, D., & van Dishoeck, E. F. 2018, A&A, 615, A83
Vorobyov, E. I. 2009, ApJ, 704, 715
Whitney, B. A., Wood, K., Bjorkman, J. E., & Wolff, M. J. 2003, ApJ, 591, 1049
Wiesenfeld, L., & Faure, A. 2013, MNRAS, 432, 2573
Williams, J. P., Cieza, L., Hales, A., et al. 2019, ApJ, 875, L9
Wootten, A. 1989, ApJ, 337, 858
Yen, H.-W., Koch, P. M., Takakuwa, S., et al. 2017, ApJ, 834, 178
Zakharenko, O., Motiyenko, R. A., Margulès, L., & Huet, T. R. 2015, J. Mol. Spectr., 317, 41

Appendix A: Formaldehyde and thioformaldehyde lines

Table A.1 provides an overview of the H_2CO, $H_2^{13}CO$, D_2CO, and H_2CS lines that have ΔJ transitions with multiple K_a transitions in the spectral coverage of the ALMA-PILS survey.

Table A.1. Line list of formaldehyde and thioformaldehyde lines.

Species	Transition	Spin isomer	Frequency (GHz)	$\log(A_{ul})$ (s^{-1})	E_u (K)	Used in analysis	Dataset	Notes
H_2CO	$5_{0,5}$–$4_{0,4}$	para	362.736	−2.863	52	–	2013.1.00278.S	
	$5_{1,5}$–$4_{1,4}$	ortho	351.769	−2.920	62	–	2013.1.00278.S	
$H_2^{13}CO$	$5_{0,5}$–$4_{0,4}$	para	353.812	−2.895	51	–	2013.1.00278.S	
	$5_{1,5}$–$4_{1,4}$	ortho	343.326	−2.952	61	–	2013.1.00278.S	Blended with H_2CS $10_{2,9}$–$9_{2,8}$
	$5_{2,3}$–$4_{2,2}$	para	356.176	−2.962	99	–	2013.1.00278.S	CH_2DOH at 356.176 GHz
	$5_{2,4}$–$4_{2,3}$	para	354.899	−2.966	98	–	2013.1.00278.S	
	$5_{3,2}$–$4_{3,1}$	ortho	355.203	−3.083	158	–	2013.1.00278.S	
	$5_{3,3}$–$4_{3,2}$	ortho	355.191	−3.083	158	–	2013.1.00278.S	
	$5_{4,1}$–$4_{4,0}$	para	355.029	−3.334	240	–	2013.1.00278.S	At same frequency as $5_{4,2}$–$4_{4,1}$
	$5_{4,2}$–$4_{4,1}$	para	355.029	−3.334	240	–	2013.1.00278.S	At same frequency as $5_{4,1}$–$4_{4,0}$
D_2CO	$6_{0,6}$–$5_{0,5}$	para	342.522	−2.933	58	–	2013.1.00278.S	CH_2DOH at 342.522 GHz
	$6_{1,6}$–$5_{1,5}$	ortho	330.674	−2.989	61	–	2013.1.00278.S	
	$6_{2,4}$–$5_{2,3}$	para	357.871	−2.925	81	–	2013.1.00278.S	
	$6_{2,5}$–$5_{2,4}$	para	349.631	−2.955	80	–	2013.1.00278.S	CH_2DOH at 349.635 GHz
	$6_{3,3}$–$5_{3,2}$	ortho	352.244	−3.019	108	–	2013.1.00278.S	
	$6_{3,4}$–$5_{3,3}$	ortho	351.894	−3.020	108	–	2013.1.00278.S	
	$6_{4,2}$–$5_{4,1}$	para	351.492	−3.152	145	–	2013.1.00278.S	
	$6_{4,3}$–$5_{4,2}$	para	351.487	−3.152	145	–	2013.1.00278.S	
	$6_{5,1}$–$5_{5,0}$	ortho	351.196	−3.413	194	–	2013.1.00278.S	At same frequency as $6_{5,2}$–$5_{5,1}$
	$6_{5,2}$–$5_{5,1}$	ortho	351.196	−3.413	194	–	2013.1.00278.S	At same frequency as $6_{5,1}$–$5_{5,0}$
H_2CS	$7_{0,7}$–$6_{0,6}$	para	240.267	−3.688	46	yes	2012.1.00712.S	
	$7_{1,7}$–$6_{1,6}$	ortho	236.727	−3.717	59	yes	2016.1.01150.S	
	$7_{2,5}$–$6_{2,4}$	para	240.549	−3.724	99	yes	2012.1.00712.S	
	$7_{2,6}$–$6_{2,5}$	para	240.382	−3.725	99	yes	2012.1.00712.S	
	$7_{3,4}$–$6_{3,3}$	ortho	240.394	−3.776	165	yes	2012.1.00712.S	At same frequency as $7_{3,5}$–$6_{3,4}$
	$7_{3,5}$–$6_{3,4}$	ortho	240.393	−3.776	165	–	2012.1.00712.S	At same frequency as $7_{3,4}$–$6_{3,3}$
	$7_{4,3}$–$6_{4,2}$	para	240.332	−3.860	257	yes	2012.1.00712.S	At same frequency as $7_{4,4}$–$6_{4,3}$
	$7_{4,4}$–$6_{4,3}$	para	240.332	−3.860	257	–	2012.1.00712.S	At same frequency as $7_{4,3}$–$6_{4,2}$
	$7_{5,2}$–$6_{5,1}$	ortho	240.262	−3.998	375	yes	2012.1.00712.S	At same frequency as $7_{5,3}$–$6_{5,2}$
	$7_{5,3}$–$6_{5,2}$	ortho	240.262	−3.998	375	–	2012.1.00712.S	At same frequency as $7_{5,2}$–$6_{5,1}$
	$10_{0,10}$–$9_{0,9}$	para	342.946	−3.216	91	yes	2013.1.00278.S	
	$10_{1,9}$–$9_{1,8}$	ortho	348.534	−3.199	105	–	2013.1.00278.S	Several lines at similar frequency
	$10_{1,10}$–$9_{1,9}$	ortho	338.083	−3.239	102	yes	2013.1.00278.S	
	$10_{2,8}$–$9_{2,7}$	para	343.813	−3.231	143	yes	2013.1.00278.S	
	$10_{2,9}$–$9_{2,8}$	para	343.322	−3.232	143	–	2013.1.00278.S	Blended with $H_2^{13}CO$ $5_{1,5}$–$4_{1,4}$
	$10_{3,7}$–$9_{3,6}$	ortho	343.414	−3.255	209	–	2013.1.00278.S	Blended with H_2CS $10_{3,8}$–$9_{3,7}$
	$10_{3,8}$–$9_{3,7}$	ortho	343.410	−3.255	209	–	2013.1.00278.S	Blended with H_2CS $10_{3,7}$–$9_{3,6}$
	$10_{4,6}$–$9_{4,5}$	para	343.310	−3.290	301	yes	2013.1.00278.S	At same frequency as $10_{4,7}$–$9_{4,6}$
	$10_{4,7}$–$9_{4,6}$	para	343.310	−3.290	301	–	2013.1.00278.S	At same frequency as $10_{4,6}$–$9_{4,5}$
	$10_{5,5}$–$9_{5,4}$	ortho	343.203	−3.340	419	–	2013.1.00278.S	Not detected
	$10_{5,6}$–$9_{5,5}$	ortho	343.203	−3.340	419	–	2013.1.00278.S	Not detected

Appendix B: Position–velocity diagrams

Position–velocity diagrams for H_2CO, $H_2^{13}CO$, and D_2CO are presented in Figs. B.1, B.2, and B.3, respectively.

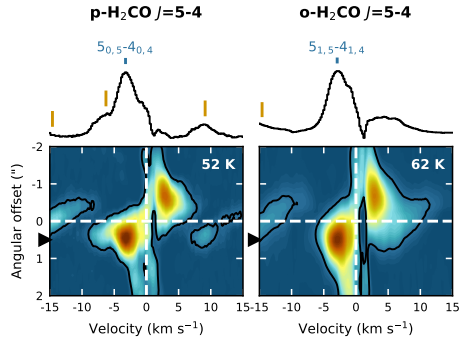

Fig. B.1. Position-velocity diagrams of the H_2CO lines along the major axis of the disk-like structure (positive angular offsets denote the north-east direction, i.e., blueshifted emission, and negative offsets denote the southwest direction, i.e., redshifted emission). The intensity (color) scale is normalized to the brightest line in each panel. The black contour denotes the 3σ contour. The dashed white lines give the source position and systemic velocity of 3.8 km s^{-1} (shifted to 0 km s^{-1}). The upper level energy is denoted in the top right corner of each panel. The spectra at $\sim$0.5″ northeast of the source (indicated by black triangles left of the vertical axes) are superimposed on the pv diagram panels. The H_2CO lines are identified by a vertical blue line, other lines by vertical orange lines.

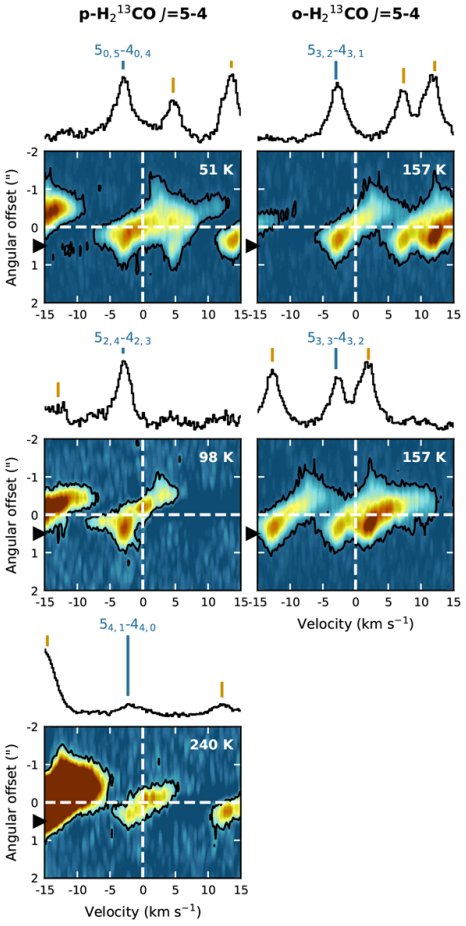

Fig. B.2. As in Fig. B.1, but for $H_2^{13}CO$.

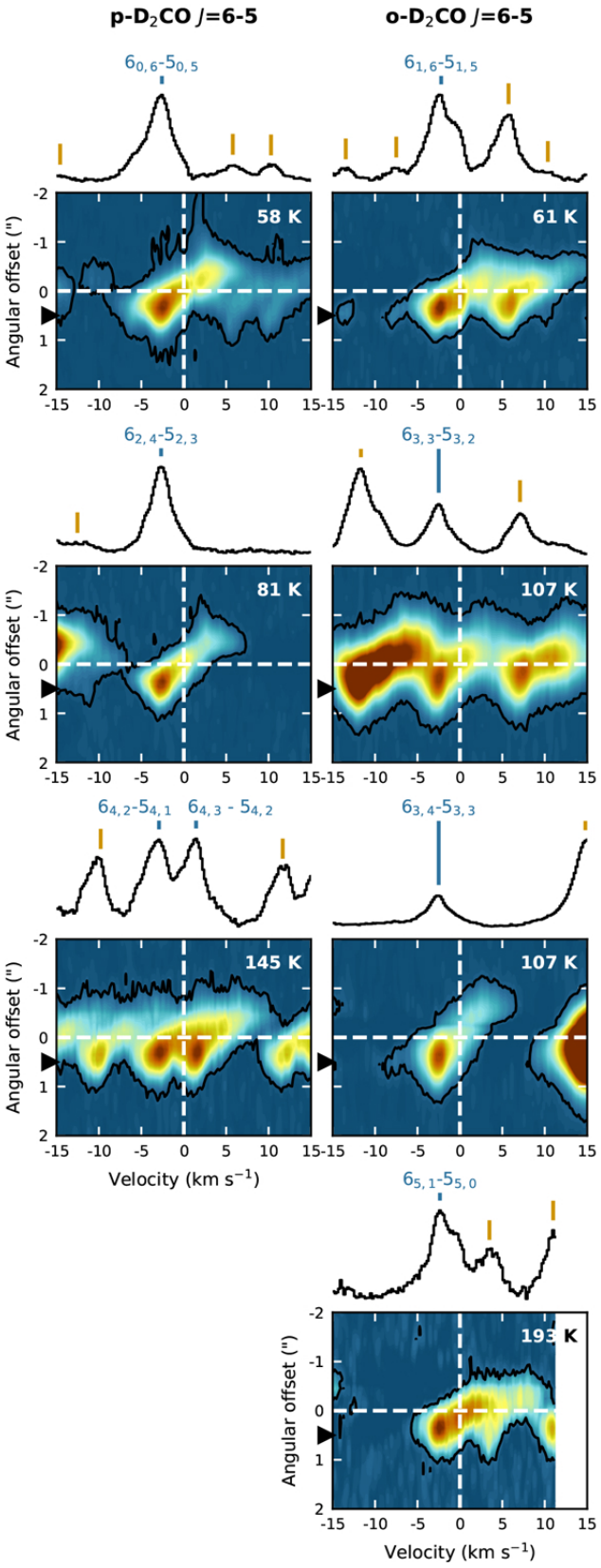

Fig. B.3. As in Fig. B.1, but for D_2CO.

Appendix C: Peak fluxes

Maps of the peak fluxes (moment 8 maps) are shown in Fig. C.1 for H_2CS and in Fig. C.2 for $H_2^{13}CO$ and D_2CO. Lines that are too blended in the central region to extract reliable peak fluxes have been excluded.

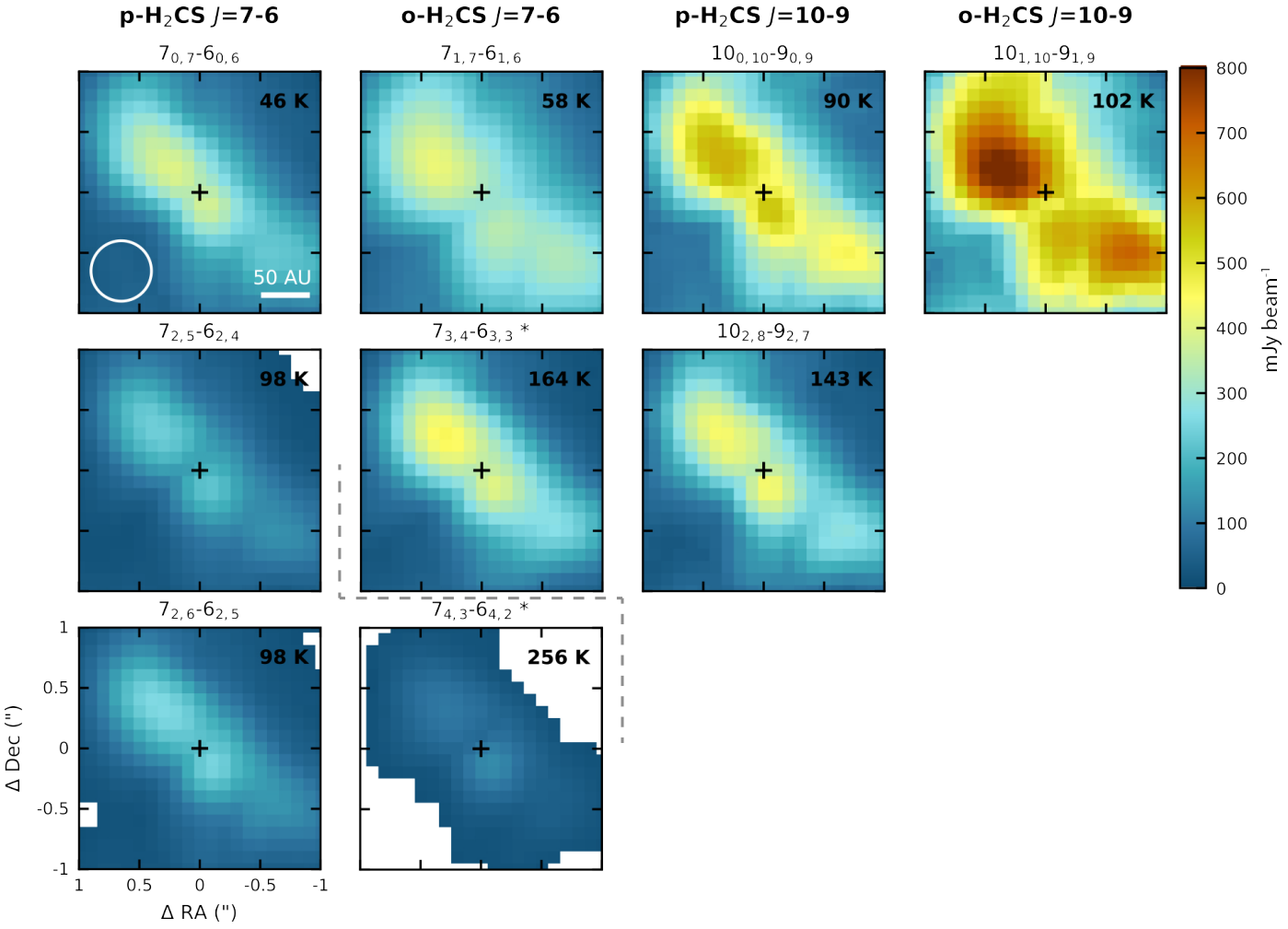

Fig. C.1. Maps of the peak fluxes (moment 8) of the H_2CS lines. Only lines for which reliable peak fluxes could be extracted in the center (i.e., that are not too blended) are shown. The transitions are denoted above the panels and the corresponding upper level energies are listed in the top right corner of each panel. Asterisks (∗) behind the transition indicate that the flux is coming from two lines with the same J and K_a level located at the same frequency (see Table A.1 for details). All panels are shown at the same intensity (color) scale for comparison. Pixels with no emission $>3\sigma$ are masked out. The continuum peak position is marked with a black cross and the beam is depicted in the lower left corner of the *top left panel*.

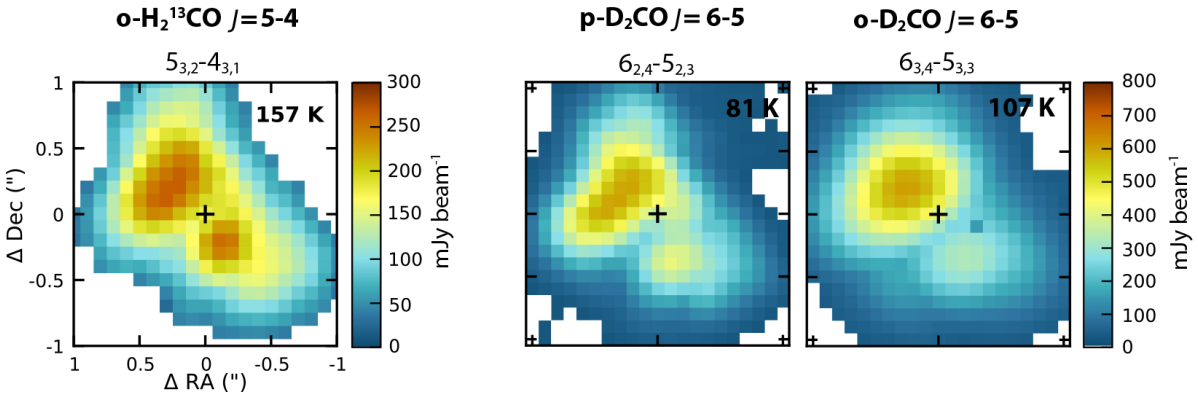

Fig. C.2. As in Fig. C.1, but for $H_2^{13}CO$ (*left panel*) and D_2CO (*middle and right panels*).

Appendix D: RADEX results for H_2CS

H_2CS line ratios as a function of temperature and density or temperature and column density derived from a grid of non-LTE radiative transfer calculations with RADEX are presented in Fig. D.1. Figure D.2 shows the column densities at which the different H_2CS lines become optically thick based on the same radiative transfer models.

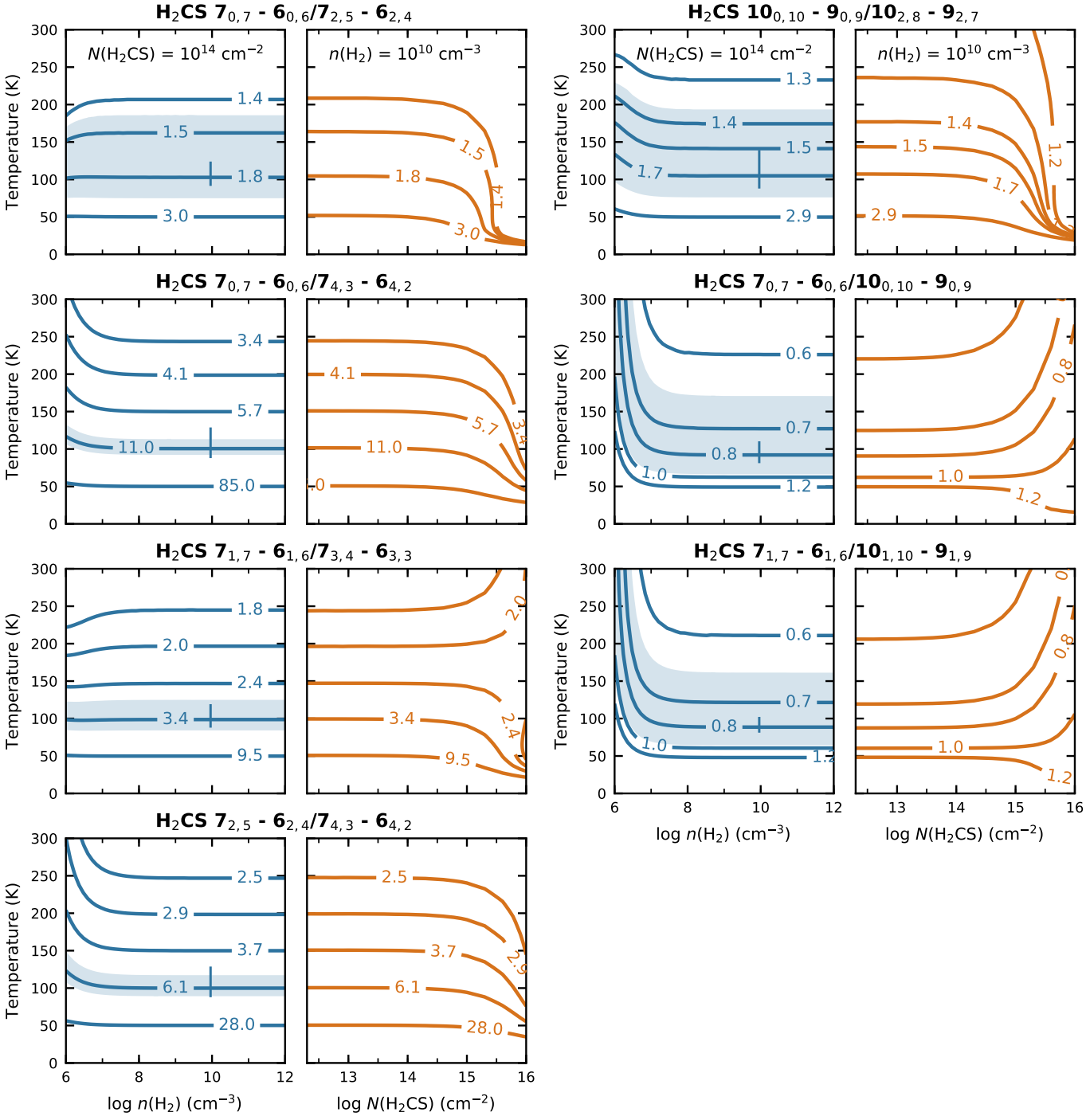

Fig. D.1. Temperature sensitivity of the H_2CS line ratios as a function of H_2 density (blue lines) and H_2CS column density (orange lines). For the density plots, a H_2CS column density of 10^{14} cm^{-2} is adopted for both o-H_2CS and p-H_2CS, and a H_2 density of 10^{10} cm^{-3} is used for the column density plots. The line ratio is listed above the panels and contours are for the ratios at temperatures of 50, 100, 150, 200, and 250 K. The blue shaded area shows the change in derived temperature if the 100 K ratio changes by 20%. The blue vertical line represents the typical 3σ error on the temperature based on the observed uncertainty in the line ratio solely due to the rms in the images. The $7_{0,7}$–$6_{0,6}/7_{2,5}$–$6_{2,4}$ ratio is equal to the $7_{0,7}$–$6_{0,6}/7_{2,6}$–$6_{2,5}$ ratio (not shown) and the $7_{2,5}$–$6_{2,4}/7_{4,3}$–$6_{4,2}$ ratio is equal to the $7_{2,6}$–$6_{2,5}/7_{4,3}$–$6_{4,2}$ ratio (not shown).

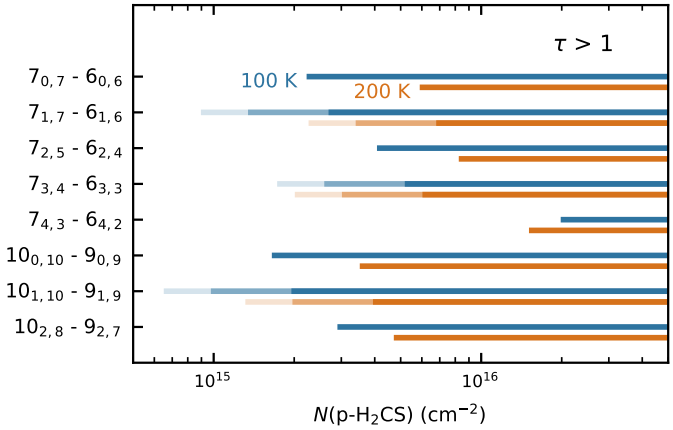

Fig. D.2. Column densities (expressed in p-H_2CS column density) at which the H_2CS lines are optically thick at 100 K (blue) and 200 K (orange) based on the non-LTE RADEX calculation. For the ortho transitions, solid dark lines assume an ortho-to-para ratio of 1, and the shaded lines assume ortho-to-para ratios of 2 and 3 (lightest shade).

Appendix E: Radial temperature profiles

Figure E.1 shows radial temperature profiles derived from H_2CS line ratios including transitions for which no collisional rate coefficients are available. These temperatures therefore result from an LTE calculation. Figure E.2 presents the radial temperature profiles based on the $7_{0,7}$–$6_{0,6}$/$7_{2,5}$–$6_{2,4}$ and $7_{0,7}$–$6_{0,6}$/$7_{4,3}$–$6_{4,2}$ ratios (Fig. 5a,c) for different position angles.

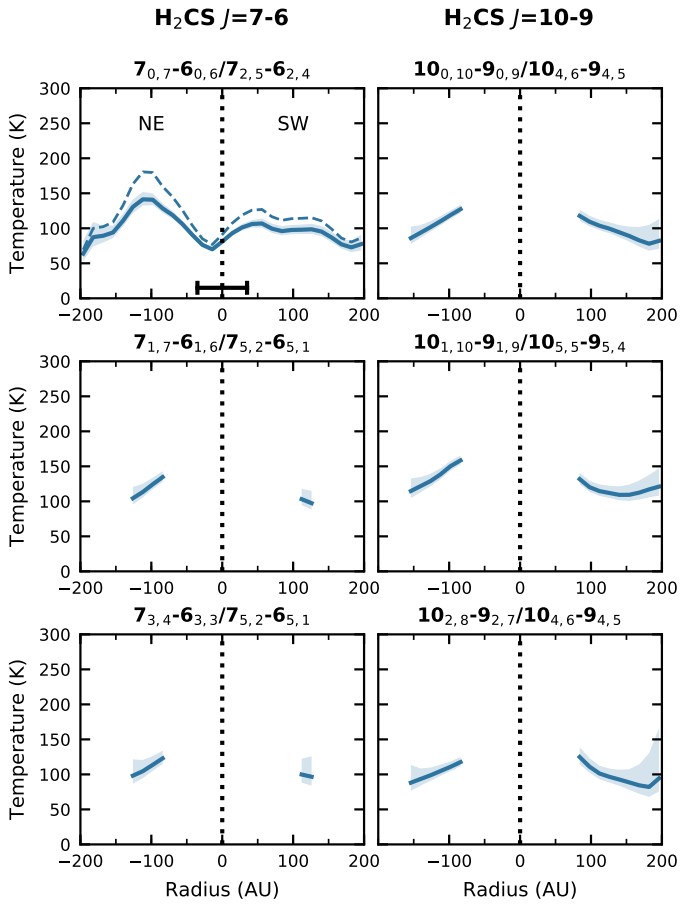

Fig. E.1. Radial temperature profiles derived from H_2CS line ratios (listed above the panels) for which no collisional rate coefficients are available. The temperature profiles are taken along the major axis of the disk-like structure (PA = 45°) and calculated assuming LTE. As a reference, the non-LTE result is also shown for the $7_{0,7}$–$6_{0,6}$/$7_{2,5}$–$6_{2,4}$ transition (dashed line in *top left panel*). The shaded area represents the 1σ uncertainty based on statistical errors. The horizontal bar in the *top left panel* gives the beam size.

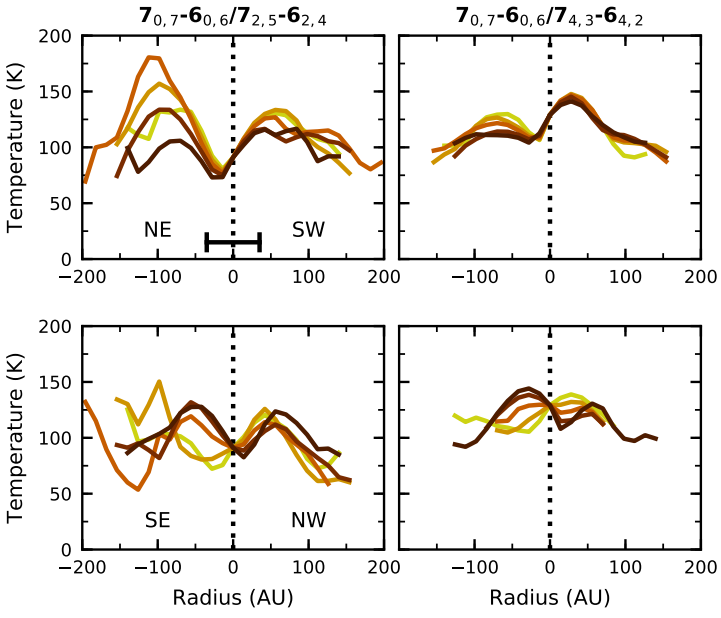

Fig. E.2. Radial temperature profiles derived from two H_2CS line ratios (listed above the panels) along different position angles (different colors) using the non-LTE RADEX results. A PA of 45° corresponds to the major axis of the disk-like structure as presented in Fig 5. The horizontal bar in the *top left panel* gives the beam size.